G Model
APCATA-15702; No. of Pages 13
ARTICLE IN PRESS
Applied Catalysis A: General xxx (2016) xxx–xxx
Contents lists available at ScienceDirect
Applied Catalysis A: General
journal homepage: www.elsevier.com/locate/apcata

Glycerol steam reforming over modified Ni-based catalysts

K. Kousi [a], N. Chourdakis [b], H. Matralis [a], D. Kontarides [b], C. Papadopoulou [a], X. Verykios [b,*]

[a] Department of Chemistry, University of Patras, GR-26504 Patras, Greece
[b] Department of Chemical Engineering, University of Patras, GR-26504 Patras, Greece

ARTICLE INFO

Article history:
Received 17 July 2015
Received in revised form
25 November 2015
Accepted 27 November 2015
Available online xxx

Keywords:
Gycerol
Steam reforming
Ni/Al_2O_3 catalysts
La_2O_3
B_2O_3
Carbon deposition

ABSTRACT

Glycerol, a by-product of biodiesel industry, could be utilized for the production of synthesis gas or hydrogen via steam reforming. Ni/Al_2O_3 catalysts are efficient for this process but could be improved regarding their activity at low temperatures, selectivity toward hydrogen production and stability with time-on stream. In the present work, the effects of addition of B_2O_3 and La_2O_3 on Ni/Al_2O_3, on the physicochemical characteristics and catalytic performance are investigated. N_2 adsorption–desorption, XRD, UV–vis DRS, TPR, NH_3-TPD and HR-TEM were employed for the evaluation of the textural and structural properties of the catalysts, while quantitative assessment of the carbonaceous deposits was performed using TPH-TPO. Catalytic behavior was investigated in the temperature range of 400–800 °C. In the absence of metal, the support presents considerable activity for the dehydration reactions and influences selectivity to oxygenate products. The catalytic behavior of the bare carriers seems to be dictated by their surface acidity.

The presence of Ni enhances significantly catalytic activity and promotes the production of gaseous products, mainly carbon oxides and hydrogen. Conversion to gas-phase products and hydrogen yield are enhanced by the addition of La_2O_3 to the support while the opposite is observed upon addition of B_2O_3. These differences are more pronounced at lower temperatures. Lower amount of graphitic carbon was formed on NiLaAl at all temperatures. However, this catalyst has not been proven more stable than the unmodified NiAl, mostly due to its poorer textural properties.

© 2015 Elsevier B.V. All rights reserved.

1. Introduction

Worldwide energy requirements are expected to triple by 2050, while the transportation sector will still depend mostly on liquid fuels [1,2]. Sustainability, energy independency and protection of the environment require the development of new technologies for the effective exploitation of renewable energy and materials resources. Nevertheless, the production of biomass derived biofuels faces serious impediments, among which feedstock availability and production costs.

Biodiesel is by far the most common biofuel used in the EU, produced via vegetable oil transesterification [3,4]. In biodiesel manufacturing, ca. 10 wt% of the processed vegetable oil is converted to crude glycerol. An interesting idea is the utilization of this crude glycerol as a raw material for hydrogen, other energy carriers and/or chemicals, having both economic and environmental advantages due to waste minimization and valorisation [5–11] . In this context, steam reforming of glycerol (SRG) has gained attention in recent years [6,9,12–21] .

SRG (Eq. (1)) is a combination of two main reactions, glycerol decomposition (Eq. (2)) and water–gas shift reaction (WGS, Eq. (3)):

$$C_3O_3H_8 + 3H_2O \leftrightarrow 3CO_2 + 7H_2 \quad \Delta H^0 = \frac{128\text{kJ}}{\text{mol}} \tag{1}$$

$$C_3O_3H_8 \leftrightarrow 3CO + 4H_2 \quad \Delta H^0 = \frac{245\text{kJ}}{\text{mol}} \tag{2}$$

$$CO + H_2O \leftrightarrow CO_2 + H_2 \quad \Delta H^0 = \frac{-41\text{kJ}}{\text{mol}} \tag{3}$$

Glycerol decomposition follows a complicated reaction network, involving several parallel and consecutive steps such as dehydration, dehydrogenation/hydrogenation, isomerization, polymerization of reaction intermediates, C—C and C—O bond cleavage [6,15,17]. Thus, the catalyst composition, texture, structure and surface properties are crucial for its efficiency. Due to the sequential reaction mechanism, operating parameters such as temperature, steam to glycerol ratio (S/G) and contact time also play a significant role [22,23].

Ni-based catalysts, especially Ni/Al_2O_3, have been proven to be active for the steam reforming of various compounds and

* Corresponding author.
E-mail address: verykios@chemeng.upatras.gr (X. Verykios).

http://dx.doi.org/10.1016/j.apcata.2015.11.047
0926-860X/© 2015 Elsevier B.V. All rights reserved.

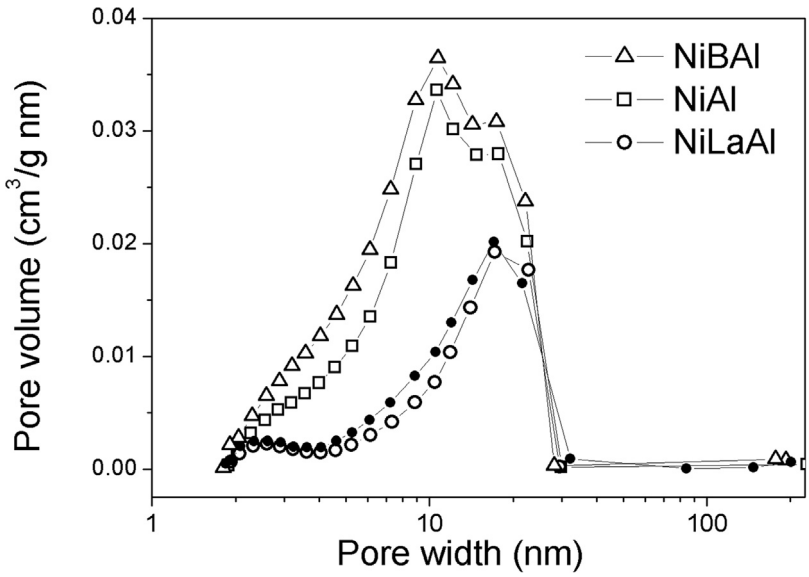

Fig. 1. Pore size distribution of the reduced NiAl (□), reduced NiBAl (△), reduced NiLaAl (○) and calcined NiLaAl (●) catalysts.

biomass derivatives (including ethanol) and they are much more cost-effective for industrial applications than noble metals [9,17]. γ-Al_2O_3 is one of the most common supports in heterogeneous catalysis due to its good textural properties and its thermal and mechanical stability. Having acid sites (mainly of Lewis type), alumina is not chemically inert, presenting catalytic properties for acid-base catalyzed reactions such as dehydration, isomerization and polymerization, that can also take place during glycerol reforming. Consequently, alumina contributes to glycerol reforming. Yet, it should have the suitable acid-base properties to promote the desired reactions but must not be too acidic to enhance cracking and carbon formation. Thus, various oxides (mainly alkaline earth oxides or lanthanide oxides have been investigated in order to improve the resistance of Ni/Al_2O_3 toward coking and metal phase sintering [16,20,24–27]. The added oxide is expected to (i) improve the stability of the metal particles at high temperature under steam (ii) weaken the Ni-alumina interaction and increase nickel precursor reducibility (iii) promote water dissociation into hydroxyl groups and spillover of these species toward the metal particles, where the decomposition of glycerol or other organic intermediates takes place, and (iv) increase the water–gas-shift reaction [20,24,25].

Lanthana has higher PZC (point of zero charge) and IEPS (isoelectric point) than alumina [28,29] and, thus, it is often used to tune the surface acidity of alumina [30–33]. In the case of glycerol gas phase dehydration, it has been reported that the addition of La_2O_3 increases the basicity and decreases the overall glycerol dehydration activity and the selectivity to acetol and acrolein [30]. According to Iriondo et al. [34], addition of lanthana reduces of acidic nature of the Al_2O_3, favoring the conversion of oxygenated hydrocarbons (OHCs) into CH_4, CO, CO_2 and H_2. They also observed that although Ni dispersion increased when La content increased, this improvement was not clearly related with catalytic activity and selectivity toward hydrogen [34]. Garbarino et al. [35] report that the reduction of the acidity due to lanthanum addition, effectively reduces the production of ethylene and other olefins. On the other hand, boron is known to increase the acidity of alumina [36–39]. Coriolo et al. [39] indicate that the addition of B_2O_3-changes the acidity of $A1_2O_3$, creating new weaker acidic sites. Therefore, it should favor the reaction paths involving dehydration steps. To our knowledge there are no literature reports on the performance of a Ni/B_2O_3–Al_2O_3 catalyst for the title reaction. There is only a study on a Ni-B amorphous alloy catalyst compared with a Raney Ni for the aqueous-phase reforming of glycerol, catalyst and conditions differing considerably with those used in steam reforming [40] .

In the present work, B_2O_3 or La_2O_3 have been added to Ni/Al_2O_3, i.e., a more acidic and a more basic oxide than alumina, respectively. The effects of a second oxide have been investigated as regards the physicochemical characteristics and the catalytic performance of Ni/Al_2O_3 catalysts for SRG. In an effort to estimate the contribution of the modified supports, alumina and the binary supports were also tested under SRG conditions.

2. Experimental

2.1. Catalysts preparation

A commercial γ-Al_2O_3 powder was used as support material. Metal oxide loadings and catalysts' synthesis methods were selected based on the results of previous studies on other reforming reactions [41–43]. $La(NO_3)_3 \times 6H_2O$ and H_3BO_3 were used as precursor compounds for La_2O_3 and B_2O_3, respectively, and were deposited on the surface of alumina by wet impregnation. Alumina was dispersed in a dilute aqueous solution of either of the above compounds and the suspension remained under stirring for one hour, followed by water evaporation and drying at 90 °C overnight. The dried materials were submitted to temperature programmed calcination (10 °C min^{-1}), the final temperature being 900 °C for the La_2O_3/Al_2O_3 which remained at the final temperature for 30 h, whereas for B_2O_3/Al_2O_3 the final temperature was 550 °C and the material remained at this temperature for 4 h. The three supports are symbolized as Al (for γ-Al_2O_3), LaAl (for La_2O_3/Al_2O_3) and BAl (for B_2O_3/Al_2O_3).

For the synthesis of $Ni/La_2O_3/Al_2O_3$ (NiLaAl), the La_2O_3/Al_2O_3 support (prepared as described above) was immersed into an aqueous solution of nickel nitrate under continuous stirring. After water evaporation, it was dried at 90 °C overnight and calcined at 600 °C for 4 h and then at 750 °C for 1 h. In contrast, the B_2O_3-modified Ni/Al_2O_3 (NiBAl) catalyst was prepared by wet co–impregnation using an aqueous solution of $Ni(NO_3)_2$ $6H_2O$ and H_3BO_3. Drying and calcination were performed following the same procedure used for the corresponding binary support. In all cases, nickel loading was 10 wt% Ni in the reduced catalyst. The prepared materials, their composition and notation are shown in Table 1.

Table 1
Materials: their notation and textural properties.

Catalysts	Notation	B_2O_3 or La_2O_3 wt% content	S_{BET} of support[a] (m^2/g)	S_{BET} (m^2/g)		Average pore diameter (nm)		Pore volume (cm^3/g)	
				Calc.[b]	Red.[c]	Calc.[b]	Red.[c]	Calc.[b]	Red.[c]
$Ni/\gamma-Al_2O_3$	NiAl	–	194	160	152	12.4	12.8	0.60	0.60
$Ni/B_2O_3-Al_2O_3$	NiBAl	5.6	205	192	185	9.2	12.2	0.53	0.68
$Ni/La_2O_3-Al_2O_3$	NiLaAl	16.8	83	83	75	16.1	16.0	0.37	0.35

[a] Specific surface area of the corresponding support.
[b] Calcined catalyst.
[c] Reduced catalyst.

2.2. Catalyst characterization techniques

Textural properties were measured based on the nitrogen adsorption–desorption isotherms at 77 K using a Micromeritics TriStar 3000 apparatus. For calculation of the specific surface areas the standard B.E.T. equation was applied within the nitrogen relative pressure range of $0.06 < P/P_0 < 0.20$. Pore size distribution was estimated based on the Barret–Joyner–Halenda (BJH) method and the adsorption branch of the isotherms.

X-ray diffractograms (XRD patterns) of the fresh and reduced catalysts were recorded on a Bruker D8 Advance diffractometer equipped with a Ni-filtered Cu Kα radiation ($\lambda = 0.15418$ nm). The following operating parameters were selected: 40 kV, 40 mA, anglerange $2° < 2\theta < 85°$, step size 0.015° and scan speed 0.3 s/step. JCPDF (Joint Committee on Powder Diffraction Standards) data files were used for the phase identification. The average size of metal crystallites was calculated following the Scherrer equation.

Diffuse reflectance spectra (DRS) of the calcined materials were recorded using a UV–vis spectrophotometer (Varian Cary 3) equipped with an integration sphere coated with $BaSO_4$. The powder materials were mounted in an appropriate quartz cell which provides an "infinite" sample thickness and the spectra were recorded at room temperature and in the range of 200–800 nm. These are presented as the Schuster–Kubelka–Munk (SKM) function $F(R_\infty) = (1 - R_\infty)^2/2R_\infty = K/S$, where R_∞ is the reflectance of a thick solid layer and K and S are the absorption and diffusion coefficients, respectively.

Surface acidity was quantified by ammonia temperature programmed desorption (NH_3-TPD). All samples were pre-reduced in order to evaluate their acidity at a similar state as they meet the reactant stream. The pre-reduced catalyst was dried overnight at 120 °C and then cooled slowly to room temperature (RT). 100 mg of the catalyst (particle size 180–250 μm) were introduced in the reactor and then reduced in situ under a stream of pure H_2 (30 mL/min) at 400 °C for 30 min and then cooled to RT under a flow of He (30 mL/min) to remove adsorbed H_2. Next, a stream of NH_3/He mixture was introduced in the reactor for 1 h, and then switched to He (30 mL/min) to remove ammonia physically adsorbed on the catalyst surface. When the signals, monitored by an MS detector (FL-9496 Balzers), were stabilized, temperature was increased from RT to 750 °C at a rate of 10 °C/min. Signal calibration was performed using known quantities of ammonia to the mass spectrometer. Integration of the TPD curves was used to quantify the amount of desorbed ammonia. With this method, the exact nature of adsorption sites (Brønsted or Lewis) can not be defined, but only the total acidity of the samples.

Reducibility of supports and catalysts was studied by temperature programmed reduction (TPR) with hydrogen. 300 mg of the material, previously dried at 393 K, was heated under a stream of 10% H_2/Ar (40 mL/min) from RT to 800 °C, with a temperature ramp of 10 °C/min. The sample remained at 800 °C under the same gas stream until the signal reached baseline (at least for 1 h). The consumption of H_2 was measured by a thermal conductivity detector (GC 8610 Chemito). A cold trap (liquid nitrogen/ethanol bath) was used to remove water from the reactor effluent before it reached the TCD detector. Various amounts of CuO were reduced under the same experimental conditions in order to calibrate the method and quantify hydrogen consumption.

High Resolution Transmission Electron Microscopy (HR-TEM) micrographs were obtained on a JEOL JEM-2100 system. For nickel particle size distributions more than 240 individual particles per specimen were measured.

2.3. Catalytic performance evaluation

The catalytic performance for the steam reforming of glycerol was evaluated following two different experimental protocols, using a fixed bed plug-flow reactor, operating at atmospheric pressure. The catalysts were submitted to ex-situ reduction. Temperature was increased gradually (10 °C/min) from RT to 800 °C under N_2 flow (50 mL/min) and then the catalyst was reduced under a stream of 100% H_2 (100 mL/min) for 1 h at this temperature, followed by cooling to RT under N_2 flow. The sample was then stored. 200 mg of the pre-reduced catalyst (particle size 180–250 μm) were reduced in situ under a stream of H_2 (50 mL/min), while temperature was increasing following a ramp of 10 °C/min, from RT to 750 °C, where it was kept for 2 h. The catalyst was then purged with helium for 15 min and temperature was increased to 800 °C and the reaction feed was introduced into the catalyst bed. The latter is prepared as follows: a mixture of 20:80 wt% glycerol/water is kept in a tank under continuous stirring at room temperature. The mixture is introduced into the evaporator using an HPLC pump. At the same time a Ar/He mixture (1:40), controlled by two separate mass flow controllers, is introduced into the evaporator from another inlet. The evaporator outlet, consisting of 20% He, 1% Ar, 75% H_2O and 4% glycerol, at W/F = 1.05 mg min mL^{-1}, is fed into the reactor. Evaporator and tubing are held at 350 °C in order to make sure that glycerol is completely in the gas phase. Catalytic activity and selectivity were assessed in the temperature range of 400–800 °C, at steady state conditions for each temperature.

Catalysts were also evaluated following a different reaction protocol, according to which catalytic tests were performed for exactly 3 h, at the temperatures of 400, 500 and 600 °C, using a fresh catalyst sample at each temperature. Activation was performed in exactly the same way as described above. Temperature was then lowered to reaction temperature and the reaction feed was introduced into the reactor (feed composition and W/F are the same as previously stated).

Feed and gas-phase reaction products were analyzed by 3 gas chromatographs: (a) a Shimadzu GC-8A, equipped with a packed Carbosieve SII column (spherical carbon molecular sieve), a TCD detector, N_2 as carrier gas and a data processor (HP 3395), (b) a Shimadzu GC-9A equipped with a packed Porapak Q column (spherical carbon molecular sieve), an FID detector, He as carrier gas and a data processor (Shimadzu C-R6A) and (c) a Shimadzu GC-14A with a packed Carboxen 1000 column (spherical carbon molecular sieve),

a TCD detector, He as carrier gas and a data processor (Shimadzu C-R6A). A cold trap was used for the condensation of the liquid products at the reactor exit before entering the gas chromatographs system. The condensed liquids were analyzed using MS-gas chromatography. In this case the gas chromatograph (Hewlett-Packard 6890), equipped with a capillary column (HP-INNOWax) and using He as carrier gas, is directly connected to the mass spectrometer (HP 5973) which is used as a detector.

One of the problems encountered in many studies is the estimation of glycerol conversion using carbon balance in the gas phase [6]. If the concentration of all carbon-containing compounds in the gas phase is not measured, this approach may be erroneous, rendering comparison between studies uncertain. This can be overcome if conversion is calculated using the moles of glycerol at the reactor inlet and outlet. In this study the total glycerol conversion (X_{tot}) and the glycerol conversion to gas (X_{gas}) were calculated following the equations:

$$X\text{tot} = \frac{[\text{glycerol}]\,\text{in} - [\text{glycerol}]\,\text{out}}{[\text{glycerol}]\,\text{in}} \times 100 \quad (4)$$

$$X\text{gas} = \frac{[\text{total Carbon}]_{\text{out, gas}}}{[\text{G}]\,\text{in}} \times 100 \quad (5)$$

$$[\text{total Carbon}]_{\text{out, gas}} = \frac{\Sigma\lfloor P_{1i}\rfloor}{3} + \frac{2 \times \Sigma\,[P_{2i}]}{3} + \Sigma\,[P_{3i}] \quad (6)$$

where P_{1i}, P_{2i} and P_{3i}, represent the product i that contains one, two or three carbon atom(s) in the molecule, respectively.

Yield was calculated based on the following:

$$Y_{P1i} = \frac{[P1i]}{3 \times [\text{glycerol}]\,\text{in}} \times 100 \text{ for 1 C containing molecules} \quad (7)$$

$$Y_{P2i} = \frac{2 \times [P2i]}{3 \times [\text{glycerol}]\,\text{in}} \times 100 \text{ for 2 C containing molecules} \quad (8)$$

$$Y_{P3i} = \frac{[P3i]}{[\text{glycerol}]\,\text{in}} \times 100 \text{ for 3 C containing molecules} \quad (9)$$

$$\Upsilon_{H_2} = \frac{[H_2]}{7} \frac{}{\times [\text{glycerol}]\,\text{in}} \times 100 \quad (10)$$

2.4. Analysis of carbonaceous deposits

The carbonaceous deposits on the spent catalysts were measured by temperature programmed hydrogenation (TPH) followed by temperature programmed oxidation (TPO). At the end of the 3 h catalytic test, the catalyst was cooled to room temperature under a flow of He (15 mL min^{-1}) to remove the unconverted reactants and products. The used catalyst was dried overnight at 120 °C and then cooled slowly to room temperature (RT). A weighted amount of catalyst was introduced in the reactor and was purged in situ with He at RT. The temperature was increased from RT to 700 °C at a rate of 10 °C/min under a reductive gas mixture of 6% H_2/He (30 mL/min) at atmospheric pressure. Temperature was kept at 700 °C until the methane signal reached the baseline. Then, it was cooled down to RT and TPO was conducted under a flow of 6% O_2/He (30 mL/min), following the same procedure. The signals of H_2, O_2, CO, CO_2 and CH_4 were continuously monitored by an MS detector (FL-9496 Balzers). Calibration was performed by introduction of known quantities of H_2, O_2, CO, CO_2 and CH_4 to the mass spectrometer. The TPH and TPO signals were integrated to calculate the total amount of carbonaceous deposits.

3. Results and discussion

3.1. Materials characterization

3.1.1. Textural properties of materials

The deposition of lanthana on the surface of γ-Al_2O_3 support resulted in an important decrease of the specific surface area (SSA) probably due to sintering during calcination and to pore blockage of the alumina pores (Table 1). On the contrary, there is no significant alteration of the textural properties upon B_2O_3 addition to γ-Al_2O_3 due to the lower calcination temperature and the lower B_2O_3 content. The same trend is followed when Ni is deposited on the surface of these carriers (Table 1). The ternary NiBAl and NiLaAl have slightly smaller SSAs than their corresponding binary supports. As materials operate in their reduced form, the textural properties were also evaluated following the reduction/activation procedure applied prior to the catalytic tests. Reduction caused a slight deterioration of texture (Table 1). From the above results it can be concluded that the oxide loading on alumina and calcination temperature are the main factors determining textural properties.

In order to clarify the impact of each of the two parameters the following observations can be made. The loading of the supported phase in the binary materials follows the order 5.6 wt% B_2O_3, 12.7 wt% NiO and 16.8 wt% La_2O_3, i.e., as the content of the supported phase increases, alumina content decreases. As it is alumina which provides the large SSA, it is logical to assume that, as its content decreases the SSA also decreases. This is true for BAl and NiAl. However, for LaAl, the decrease is much higher than expected (Fig. S1 in supporting information). The most plausible reasons for the significant textural deterioration observed for LaAl and NiLaAl is the blockage of the smaller mesopores of alumina and/or sintering during calcination. Pore size distribution confirms the above hypothesis, as can be seen in Fig. 1. NiLaAl catalyst has a higher average pore diameter, a narrower pore size distribution and a much smaller pore volume, as compared with the other Ni catalysts.

3.1.2. X-Ray diffraction analysis

The X–ray diffraction analysis of the binary supports (not shown) exhibit the characteristic features of γ-Al_2O_3 for all samples. The presence of B_2O_3 cannot be detected in the BAl support, as boron oxides are difficult to crystallize, forming amorphous glassy phases [43]. On the contrary, new phases were detected in the X-ray diffractogram of LaAl. The sharp and narrow peaks observed at 2θ of 23.46°, 33.41°, 41.20°, 47.98°, 54.11° and in the range of 70–81° are attributed to $LaAlO_3$ in rhombohedral symmetry (JCDD #31-0022). The formation of this phase is expected after calcination at 900 °C [44,45]. The existence of La_2O_3 cannot be excluded but it is difficult to be confirmed as its main diffraction peaks are overwhelmed by those of alumina. The formation of $LaAlO_3$ may be another reason for the notable decrease in SSA.

XRD patterns of calcined NiAl and NiLaAl (not shown) exhibit the characteristic peaks due to X-rays diffraction by the NiO cubic lattice, reflections being more intense for NiLaAl. On the contrary, crystalline NiO are not clearly seen in the XR diffractogram of calcined NiBAl. The boron content and the preparation procedure of this catalyst results in improved dispersion of nickel oxide, the crystallites of the latter being beyond the detection limits of the XRD technique [43] . The existence of $LaNiO_3$ in NiLaAl cannot be confirmed as its diffraction pattern is very similar to $LaAlO_3$ that has been detected on the calcined support. However, according to Palma et al. [46] the similarities between the lattice parameters of $LaNiO_3$, $NiAlO_3$ and the (1 1 0) plane of the γ-Al_2O_3 favor the formation of either a $NiLaO_3$ perovskite monolayer on top of the $LaAlO_3$ perovskite or $LaNi_{1-x}Al_xO_3$ mixed oxide phase. The presence of $NiAl_2O_4$ is also difficult to verify as lattice parameters are

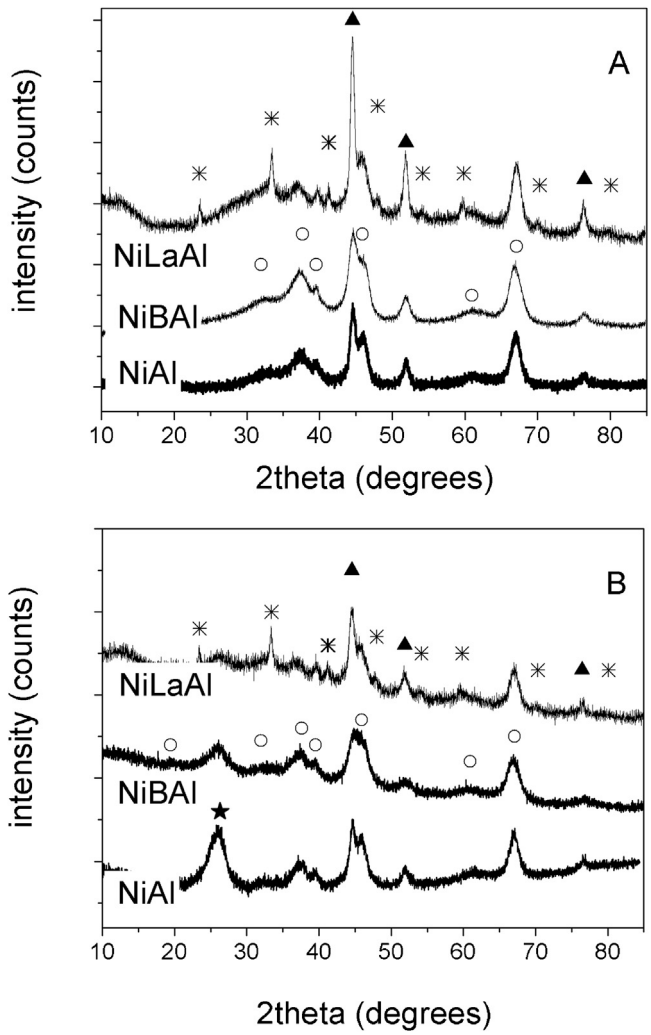

Fig. 2. The XRD patterns of Ni-catalysts (A) reduced and (B) used at 400 °C, ○ γ-Al_2O_3 (JCPDS 10-0425), * $LaAlO_3$ (JCPDS 31–0022), ▲ Ni (JCPDS 04-0850), ★ graphitic C (JCPDS 41–1487).

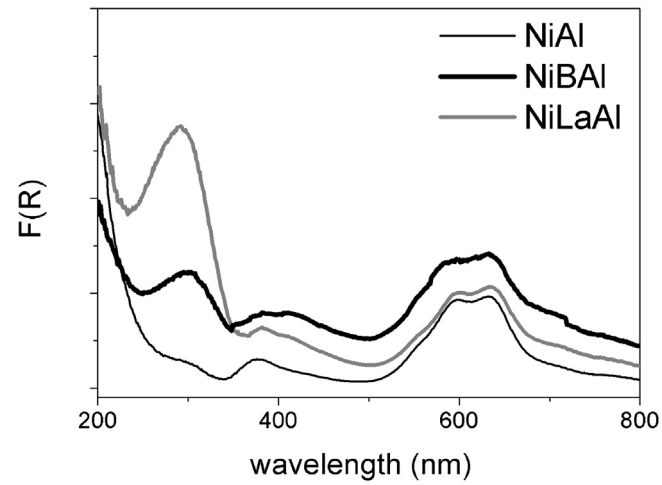

Fig. 3. The UV–vis DR spectra of the Ni-catalysts recorded after calcination using alumina as background.

comparable to those of γ-Al_2O_3 and thus diffraction peaks overlap those of the support.

The XR diffractograms of the reduced Ni-catalysts are presented in Fig. 2A. $LaAlO_3$ or other orthorhombic perovskite phase is still present in the reduced NiLaAl, accompanied by diffraction peaks due to γ-Al_2O_3 and metallic nickel, in accordance with the results of Palma et al. [46]. The different degree of dispersion of the nickel oxide, observed for the calcined catalysts, resulted in significant differences in the Ni^0 dispersion after reduction; i.e., the intensity of the peak corresponding to X-ray diffraction from (1 1 1), (2 0 0) and (2 2 0) planes of Ni^0, appearing at 44.55°, 51.89° and 76.45° Bragg angles respectively, follow the order NiBAl < NiAl < NiLaAl (Fig. 2). The average Ni particle size, calculated from the diffraction peak of the Ni (2 0 0) plane (at $2\theta = 51.9°$), using the Scherrer equation, give a quantitative measure of this observation (Table 2).

3.1.3. UV–vis DRS analysis

The UV–vis DR spectrum of γ-Al_2O_3 (Fig. S2) shows an absorption band in the area 200–350 nm with maximum at ca. 220 nm, which is attributed to the ligand-metal charge transfer transitions from $O^{2-} \rightarrow Al^{3+}$ [47] . The absorption edge has been calculated to be 3.99 eV, in accordance with the formation of γ-Al_2O_3 [48]. The DR spectrum of LaAl sample presents an absorption band with at least two maxima, one at about 206 nm and one at 230 nm (Fig. S2). Besides the $O^{2-} \rightarrow Al^{3+}$ charge transfer transitions in γ-Al_2O_3, other electron transitions also contribute to this absorption band. An absorption band due to $O^{2-} \rightarrow La^{3+}$ charge transfer transition is also expected in this area. Barrera et al. [45]. observed a shift to higher wavelength in the binary La-Al oxides. In fact, they suggest alterations of the coordination shell of the Al^{3+} cations due to the interactions with the La^{3+} cations [45]. In addition to the formation of $LaAlO_3$, the inter-diffusion of Al^{3+} and La^{3+} ions between $LaAlO_3$ and Al_2O_3 solid phases results in the formation $LaAl_{11}O_{18}$ microdomains, i.e., the electronic environment of Al^{3+} and La^{3+} ions can vary considerably and these variations can be expressed by the observed shift in the absorption band [45]. The absorption edge of LaAl increases to 4.34 eV, in line with literature reports [47,48]. The DR spectra of BAl shows two bands, a band at the detection limits (200 nm) and a broad band at ca. 255 nm. The presence of the two distinct bands may indicate at least two different electronic environments for Al^{3+}, due to the presence of B^{3+} ions. To our knowledge there are no literature reports on UV–vis DRS studies on borated aluminas and further investigation of this issue is beyond the scope of the present study.

The UV–vis electronic spectra of Ni-catalysts are much more complicated due to the influence of neighboring metal ions and more remote ligands, providing information on the coordination environment of the transition cations. In an effort to gain more information on the symmetry and the coordination of nickel species, the DR spectra of the calcined Ni-catalysts were recorded using as reference the alumina support (Fig. 3). The absorbance in the 250–350 nm region is assigned to $O^{2-} \rightarrow Ni^{2+}$ charge-transfer in octahedral symmetry in a NiO lattice [49,50]. The maximum has been reported to be at 320 nm in bulk NiO and it is blue shifted in supported NiO/Al_2O_3 catalysts [43,49,51–53]. A peak at λ < 250 nm and a shoulder at about 294 nm is observed in the spectrum of NiAl catalyst, indicating good dispersion of the nickel oxide and interaction with the alumina support [51,53 and citations therein]. More intense bands at ca. 294 nm are observed for the NiBAl and NiLaAl samples (Fig. 3), implying different Ni^{2+} electronic environment and/or larger NiO particles. For NiBAl, the difference in this band must be related to alterations of $O^{2-} \rightarrow Ni^{2+}$ charge-transfer transition due to the presence of B_2O_3, as Ni^{2+} and B^{3+} precursors were co-impregnated and, thus, may have formed a ternary amorphous common phase [43]. This is in accordance with the XRD results by which no nickel phase could be clearly detected for the calcined NiBAl catalyst, indicating small NiO particles. For NiLaAl, the absorption band at ca. 294 nm is more important and may be due to both reasons. XR diffractograms

Table 2
Average nickel particle size (estimated by XRD) after reduction and catalytic tests for 3 h at 400 °C, 500 °C and 600 °C and carbonaceous deposits after testing for 3 h at 500 °C.

Catalysts	$d_{Ni,R}$ (nm)	$d_{Ni,U400C}$ (nm)	$d_{Ni,U500C}$ (nm)	$d_{Ni,U600C}$ (nm)	$d_{Ni,U\ stability}$ (nm)	H_2 consumption (mmol H_2/g_{cat})	$C_{500\,°C}$ (mg C/g_{cat})
NiAl	9.5 ± 0.5	7.6 ± 0.4	7.6 ± 0.4	8.4 ± 0.7	16.1 ± 0.7	0.91	121
NiBAl	6.7 ± 0.2	4.3 ± 0.4	4.3 ± 0.4	4.8 ± 1.0	–	1.18	181
NiLaAl	11.7 ± 0.4	10.7 ± 0.7	10.7 ± 0.7	10.6 ± 0.5	14.2 ± 0.6	0.85	39

show larger Ni^0 crystallites for the reduced NiLaAl catalyst, as compared to those in NiAl. On the other, hand, the calcination of NiLaAl catalyst is expected to enhance the diffusion of Ni^{2+} into the $LaAlO_3$ lattice, creating a different electronic environment than in NiAl.

The band at 370–385 nm, corresponding to d-d electron transitions in octahedral Ni^{2+} in NiO lattice, is clearly observed for all catalysts and differences are insignificant (Fig. 3). An overlapping band with maximum at ca. 410 nm is observed for the NiBAl catalyst, attributed to octahedral Ni^{2+} in $NiAl_2O_4$-like surface spinel, having different physical and catalytic properties than bulk nickel aluminate [54,55]. This band is more intense for Ni/B_2O_3–Al_2O_3 catalysts calcined at lower temperatures [43] but calcination at 750 °C enhances the diffusion of Ni^{2+} into the alumina lattice, to occupy tetrahedral coordination in the bulk $NiAl_2O_4$-spinel [35]. The latter species are detected by the presence of the doublet in the area 500–650 nm. The formation of this phase is also confirmed for NiAl and NiLaAl as the calcination temperature is the decisive factor for its formation.

In summary, NiAl exhibits the properties of a state of the art Ni/Al_2O_3. NiO and $NiAl_2O_4$ are present in all calcined catalysts. B_2O_3 and NiO addition do not alter considerably the textural properties of the support but an important decrease in SSA and porosity is observed upon La_2O_3 introduction. This must be mainly due to the formation of $LaAlO_3$ phase. After reduction, differences are observed in Ni^0 dispersion, being greater in NiBAl and lower in NiLaAl, as a result of the lower SSA of LaAl.

3.1.4. Estimation of surface acidity

Glycerol decomposition reactions can follow different paths, also involving dehydration reactions [15]. Since the latter are catalyzed by materials having acid-base activity [30,56], the acidity of the catalysts can be investigated using NH_3 adsorption–desorption [57,58]. The NH_3-TPD profiles of the reduced Ni-catalysts are exhibited in Fig. 4a. The Ni-catalysts were studied after reduction, in the state that these operate under glycerol reforming conditions. Only NH_3 could be detected during TPD, indicating that adsorption and desorption of ammonia take place molecularly. An intense desorption peak is observed at about 100 °C for the NiAl catalyst (Fig. 4a), similar in shape to that obtained for the alumina support (not shown) [59] but lower in intensity and shifted to lower temperature by about 15 °C. This is probably due to the higher calcination temperature and the reduction that proceeded. Desorption of ammonia is observed to continue at higher temperatures, the higher amount being released up to 400 °C and then forming a decaying "tail". The addition of La_2O_3 on alumina results in a decrease of the total amount of desorbed ammonia, being more important for the stronger acid sites (higher desorption temperature) while the presence of Ni^0 had no further effect (Fig. 4b). On the contrary, much higher acidity is exhibited by NiBAl and BAl (Fig. 4a and b). Although the acidity of NiBAl is significantly lower than that of BAl, NiBAl is still more acidic than the other catalysts. The more important difference between NiBAl and the other catalysts is observed for the weak acid sites, as those desorbing ammonia up to 300 °C. The results of NH_3 TPD analysis are in accordance with relevant literature studies, showing decrease in acidity upon La_2O_3 addition [28,30,31] and the contrary in the presence of B_2O_3 [36,38].

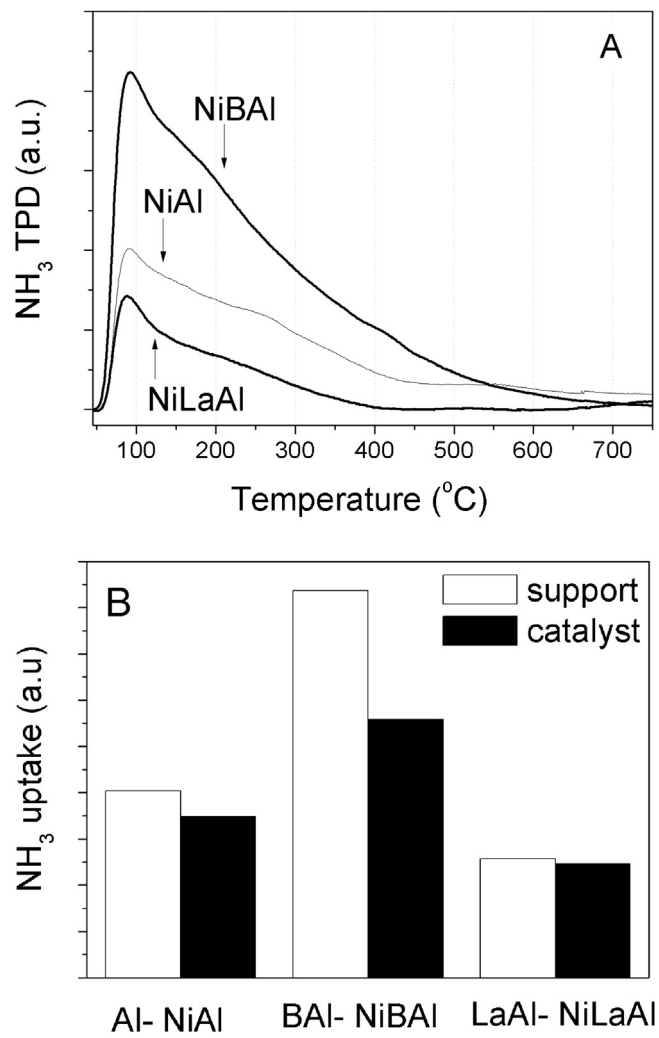

Fig. 4. NH_3-TPD profiles obtained over the reduced Ni-catalysts (A) and relative acidity of catalysts and supports (B).

3.1.5. Reducibility of catalysts

The reducibility of the catalysts was evaluated via H_2-TPR (Fig. S3). The supports have negligible reducibility. For Ni-catalysts, hydrogen consumption starts at about 650 °C for NiAl and NiLaAl and at 600 °C for NiBAl and increases sharply up to 800 °C. The main reduction takes place isothermally at 800 °C. Although the hydrogen consumption profiles are comparable regarding their shape to those obtained by other similar Ni/Al_2O_3 catalysts [43,58], reduction takes place at higher temperatures (by about 120–130 °C) whereas total hydrogen consumption is lower than that of similar catalysts calcined at lower temperatures [43]. Reduction profiles similar in shape and recorded at temperatures higher than 750 °C was also reported by Bizkarra et al. [60], who have calcined their materials at 700 °C for 4 h. Palma et al. [46] , studying Ni/La_2O_3–Al_2O_3 catalysts calcined at 900 °C, report that catalysts' reduction occurs in a single step with a maximum in the reaction rate at ca. 860 °C. The complete reduction of NiO (assuming that this is the main nickel phase in all calcined catalysts) would require

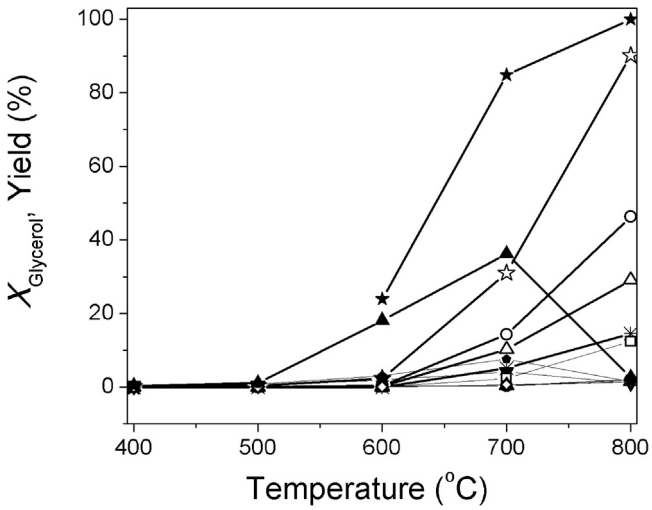

Fig. 5. Conversion of glycerol and yields (*Y*%) of main gas products in the absence of catalyst. ★ total conversion%, ☆ conversion to gas%, * *Y*% hydrogen, ○ *Y*% CO, ● Y% CO_2, ▲ *Y*% acrolein, ⬟ *Y*% acetol, ▼ *Y*% acetaldehyde, □ *Y*% methane, △ *Y*% ethylene, ◇ *Y*% propane.

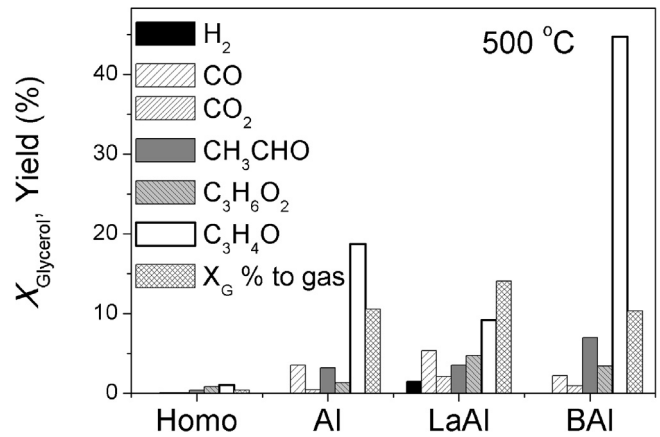

Fig. 6. Conversion of glycerol and yields (Y %) of main gas products obtained with the supports at 500 °C.

1.70 mmol H_2/g_{cat}. As it can be seen in Table 2, the total amount of hydrogen consumed is significantly lower. Similar decrease in reducibility was also reported by other researchers [61,62]. The main reason for the hindrance of reducibility may be due to stronger interactions of "nickel oxide entities" with the support. It has been suggested that these enhanced interactions are the result of Ni^{2+} cations occupying Al^{3+} in the γ-Al_2O_3, in the $LaAlO_3$ or in a $La_xAl_yO_z$ lattice or the reverse, i.e., the incorporation of Al^{3+} or La^{3+} into NiO lattice [46,61–64]. Calcination temperature plays an important role; the higher the calcination temperature the lower the reducibility [61]. As the calcination temperature increases, the diffusion of Ni^{2+} ions into the γ-Al_2O_3 spinnel to form $NiAl_2O_4$ is promoted. It is known that the latter phase is difficult to reduce. Previous studies on similar materials have shown much higher reducibility for Ni/Al_2O_3 calcined at 550 °C instead of 750 °C (applied in the current study) [43]. The H_2-TPR analysis results are in accordance with those of UV–vis DRS (Fig. 3) that confirms the existence of Ni^{2+} in tetrahedral symmetry (doublet at 500–650 nm) as in $NiAl_2O_4$. Blom et al. [61]. observed lower reducibility of Ni/La_2O_3–Al_2O_3 as compared to Ni/Al_2O_3 even though these catalysts were calcined at the same temperature (900 °C). Regarding the NiLaAl, there may be other explanations for the difficulty regarding reducibility. The interaction between nickel and lanthana oxidic species may lead to incomplete reduction due to La^{3+} ions incorporated into the surface of NiO species, creating the decoration phenomenon [62,65]. For perovskite ABO_3 structures, the nature of the B metal cation determines the formation of the oxygen vacancies [46]. If the B cation is hardly reducible as Al^{3+}, oxygen vacancies occur at very high temperatures. According to Palma et al. [46] morphological constrains induced by γ-Al_2O_3 support on the perovskite layer and the random distribution of Ni and Al at the B sites of the perovskite prevents oxygen vacancies to group. Consequently, nickel reduction takes place only at high temperatures [46].

3.2. Catalytic performance experiments

The boiling point of glycerol is 290 °C, while its evaporation is accompanied by decomposition. Thus, its homogeneous reactions were investigated in the temperature range of 400–800 °C. As it can be seen in Fig. 5, in the absence of catalyst, higher than 20% total glycerol conversion can be achieved at temperatures <600 °C, increasing considerably at higher temperatures, whereas almost total decomposition of glycerol is observed at 800 °C, most of the products being in the gas phase at this temperature. At temperatures between 400 and 600 °C, the main products are oxygenates as acetol (1-hydroxy-2-propanone), acrolein (prop-2-enal), acetaldehyde, acetone, acetic acid and others in smaller quantities, such as phenol and compounds with C > 3, showing that homogeneous polymerization also occurs. An interesting observation is that acrolein is the main product and its yield increases with temperature up to 700 °C, while it is negligible at higher temperatures. At $T > 700$ °C, more severe decomposition occurs, resulting in the formation of methane ($Y_{800} = 12.4\%$), ethylene ($Y_{800} = 29.0\%$) and propane ($Y_{800} < 2\%$), CO ($Y_{800} = 46.3\%$), CO_2 ($Y_{800} < 2\%$) and hydrogen ($Y_{800} = 14.6\%$) while other hydrocarbons are also present (Fig. 5).

The evaluation of the catalytic performance of the carriers was studied in the temperature range of 400–800 °C but important differences are observed at lower temperatures. At 400 °C, alumina (Al) does not exhibit any significant activity, increasing only slightly the conversion to gaseous products compared to that observed homogeneously. LaAl and BAl are much more active, total conversion of glycerol being 85% and 100% respectively, while acrolein is the main product of BAl ($Y_{400,acrolein} = 38.5\%$) at 400 °C. Raising temperature to 500 °C results in 100% total conversion for all supports, which is 300 °C lower than that achieved homogeneously. Glycerol conversion to gas phase products (X_{gas}) and yield to major products at 500 °C are shown in Fig. 6. Alumina favors dehydration reaction pathways, the main product being acrolein ($Y_{500,acrolein} = 19\%$), whereas a 10% conversion to gas-phase products (mainly CO, CO_2 and acetaldehyde) is observed. Addition of boron does not improve activity toward gas phase products but has a remarkable effect on selectivity to acrolein, increasing its yield to 45% (Fig. 6). Acetol and acetaldehyde yields are also increased. Addition of La_2O_3 to alumina has the opposite effect. Conversion to gaseous products increases to 15%, the yield of acetol is also increased while acrolein production is considerably suppressed, as compared to alumina. The yields of CO and CO_2 also increase. At this temperature, H_2 obtained by all supports is negligible.

Solid acids are good catalysts for the dehydration of glycerol, one of the main products being acrolein [11,66]. According to Tsukuda et al. [66], dehydration with the elimination of secondary hydroxyl group of glycerol forms 3-hydroxypropanal. The latter, being unstable, is readily dehydrated into acrolein [66]. Stosic et al. [30]. have shown that the route of glycerol dehydration to acrolein is preferentially catalyzed by materials exhibiting Brönsted acidity, in line with the suggestion of Tsukuda et al. [66]. who imply the protonation of the secondary hydroxyl group of glycerol before water removal to form 3-hydroxypropanal. Alu-

mina exhibits mainly Lewis acidity. B_2O_3–Al_2O_3 materials possess considerable Brönsted acidity, related to the boron content [67]. Our results are in line with the literature as acrolein formation not only follows the same order with that of surface acidity, i.e., LaAl < Al < BAl but these are linearly connected (Fig. S4).

Another possible route for glycerol dehydration involves the elimination of a terminal hydroxyl group, forming acetol (1-hydroxyacetone). Hernandez et al. [11], studying glycerol dehydration at 400 and 500 °C over $LaNiO_3$ and La_2O_3 in the absence of steam, report the formation of acetol but no acrolein was detected under their reaction conditions. Interestingly, glycerol conversion and selectivity to products at 400 and 500 °C are similar for both catalysts ($LaNiO_3$ and La_2O_3, reduced or not), including the formation of CO_x (mainly CO). This leads to the conclusion that active sites for the glycerol conversion are not necessarily based on Ni^0, but it is the basicity of the catalysts (oxygen anion sites) which is the key parameter to form acetol and even break C—C bonds to a certain extent [11]. Auroux and co-workers [10,30]. have observed that basic sites are important for acetol formation. Our results are in accordance with the above studies, as LaAl gives higher yield of acetol, CO and CO_2 than Al and BAl (Fig. 6). Regarding acetaldehyde formation there is no general consensus. It may be produced via partial decomposition of 3-hydroxypropanal, with CO and H_2 removal, as concluded by Tsukunda et al. [66]. In contrast, Pompeo et al. [15]. and Pathak et al. [8] . suggest that acetaldehyde is formed from acetol. Our results show higher acetaldehyde formation for the materials that also give higher acrolein yield, indicating that the path of acetaldehyde formation through 3-hydroxypropanal is more probable. A schematic representation of the reaction paths for the oxidic materials studied is given in Scheme 1.

Ni-based catalysts were also evaluated at the temperature range of 400–800 °C. In the presence of Ni, catalytic activity is greatly improved as compared to the bare supports (Fig. S5). At 400 °C, 100% total conversion is achieved by NiAl, whereas glycerol conversion to gas is increased from 10% for Al to 30% for NiAl. The usual oxygenates (mainly acrolein, acetaldehyde, acetol, acetone) are observed. As Ni^0 catalyzes the cleavage of C—C bonds, more CO (Y_{CO} = 5%) and CO_2 $\left(Y_{CO_2} = 16\%\right)$ are formed while the yield of hydrogen is 13.5% at 400 °C. Conversion to gas products increases with temperature and so do yields of hydrogen and carbon oxides. It is worth noting that CO_2 yield increases up to 600 °C, decreasing at higher temperatures while the yield of CO increases with temperature. This is expected as the inverse WGS reaction is favored at high temperatures. In the presence of B_2O_3, conversion to gas and hydrogen yield is higher at 400 °C but at higher temperatures it is similar to that achieved by NiAl (Fig. S5). Selectivity toward acrolein over NiBAl is high at this temperature (not shown). On the other hand, La_2O_3 does not seem to have any important effect on conversion to gas or products selectivity at 400 °C, but H_2 and CO yields are a little higher at higher temperatures. The CO/CO_2 molar ratio exhibits an interesting minimum at 500 °C (Fig. S5C), indicating that these catalysts perform as high temperature WGS catalysts. Overall, differences among the three catalysts are very small at temperatures higher than 600 °C since, at this temperature essentially complete conversion to gas phase products is achieved and product distribution is mostly governed by thermodynamics.

Catalysts were further investigated at 400, 500 and 600 °C, at which temperatures their differences are most pronounced. Catalytic tests were performed for 3 h at each temperature, using a new catalyst sample each time, in order to also evaluate coking behavior following an identical time on stream. The obtained results are presented in Fig. 7. Interestingly, these are not quite the same as those observed with the previous protocol which involved continuous reaction following a descending temperature order, with the same batch of catalyst. At 400 °C, NiAl and NiLaAl fresh samples exhibit higher glycerol conversion to gas phase products (Figs. 7 and S5). The most probable explanation is that in the previous protocol (Fig. S5), 400 °C was the last temperature at which the catalysts were studied and a certain deactivation may have occurred. Yields of H_2, CO and CO_2 follow the same trend as previously observed (Fig. 7A and B), the catalysts exhibiting reasonable glycerol conversion to gas-phase products and high WGS activity. At 400 °C,

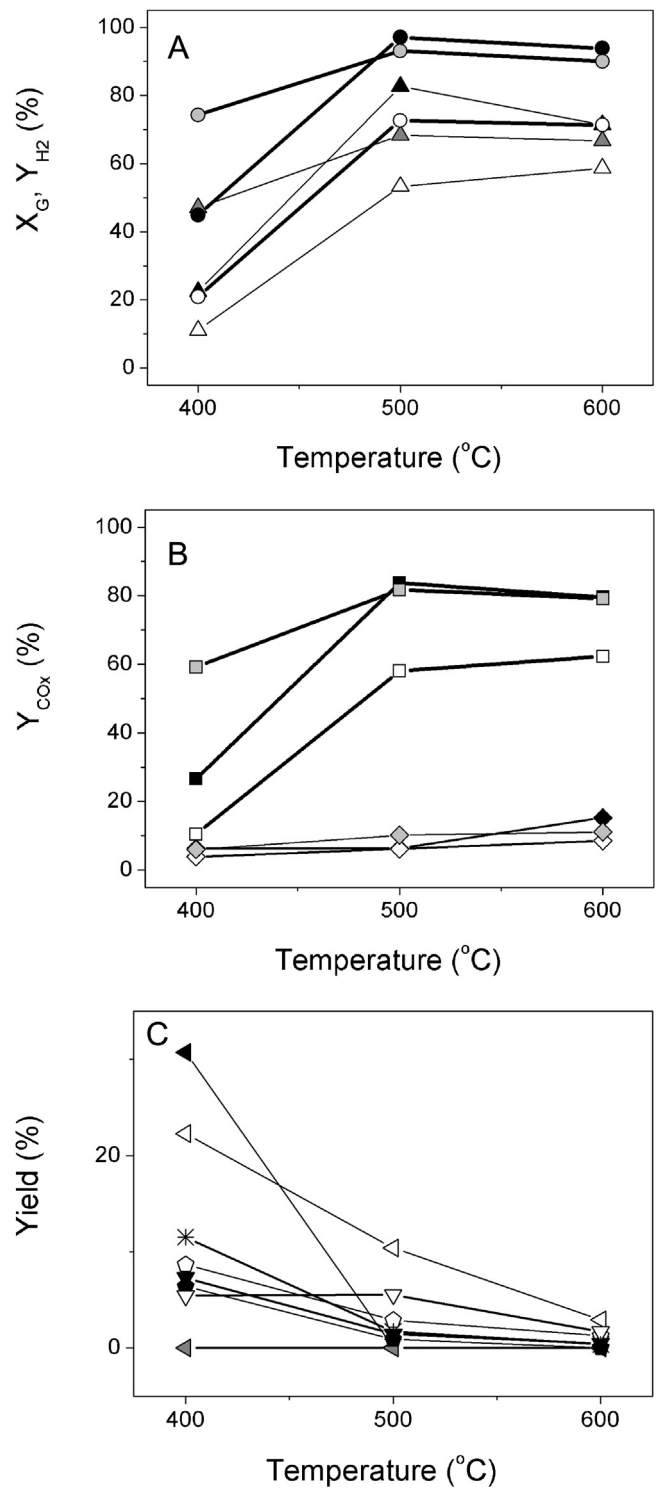

Fig. 7. Conversion to gas products and yields% of main products achieved over NiAl (black symbols), NiBAl (white symbols) and NiLaAl catalysts (gray symbols), using a fresh catalyst at each temperature. (A) ○ X_{gas} of glycerol, △ Y_{H_2}%, (B) ◇ Y_{CO}% and □ Y_{CO_2}% and (C) ◁ $Y_{acrolein}$%, ⬟ Y% acetol, ▽ Y% acetaldehyde, * Y% methane for NiLaAl.

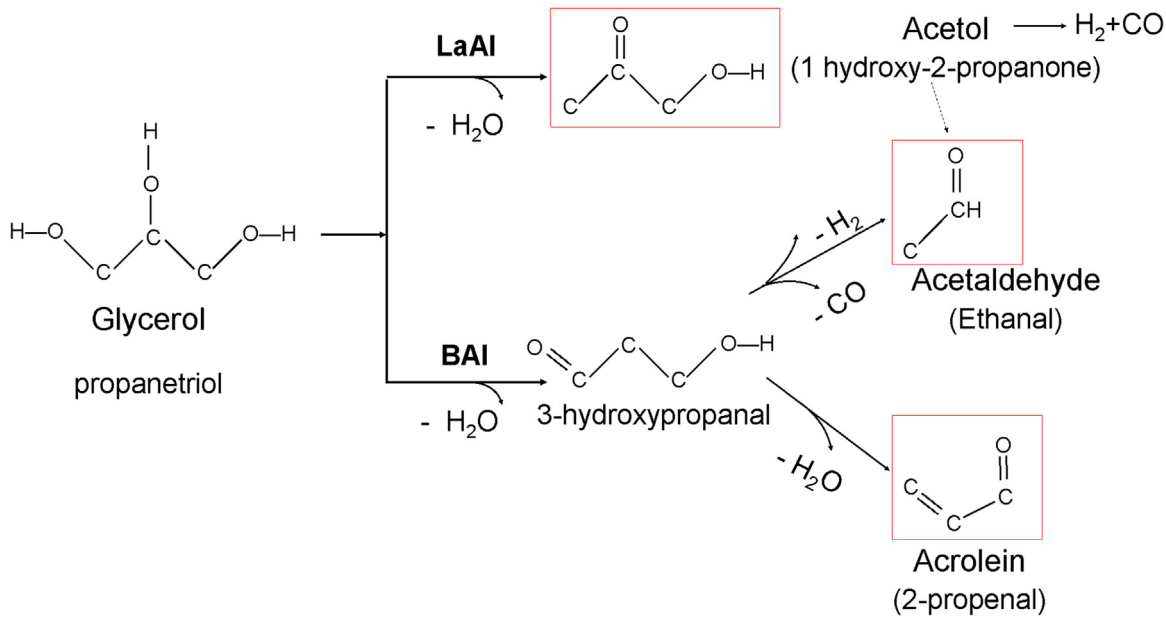

Scheme 1. Reaction pathways of steam reforming of glycerol over modified aluminas with different acidity.

NiLaAl is the best catalyst as it gives not only higher hydrogen yield (Y_{400}, H_2 = 47%) but also higher CO_2 yield (Y_{400}, CO_2 = 59%). For these low reaction temperatures, interesting differentiations regarding the yields of oxygenate can be seen (Fig. 7C). For NiAl, the yield of acrolein at 400 °C is 31% but it is negligible at higher temperatures. In the presence of B_2O_3, acrolein is present in the products at all temperatures. A $Y_{400,acrolein}$ = 22% is obtained over NiBAl at 400 °C, decreasing to 10% at 500 °C and 3% at 600 °C (Fig. 7C). A 5–7% yield of acetaldehyde is also obtained over NiAl and NiBAl in the temperature range of 400–600 °C. Yield of acetol is ca. 7% over NiAl and 9% for NiBAl at 400 °C and negligible for all catalysts at higher temperatures. Yields of acrolein and other oxygenates are negligible over NiLaAl at all temperatures. On the contrary, methane is formed (Fig. 7C) at 400 °C (Y_{400}, CH_4 = 12%). In summary, B_2O_3 addition favors dehydration and the production of oxygenates, whereas in the presence of La_2O_3 the cleavage of C—C bonds are favored even at 400 °C. At 500 °C and 600 °C any other product besides H_2, CO and CO_2 is practically absent over NiAl and NiLaAl, but NiBAl still produces acrolein ($Y_{500,acrolein}$ = 10.4%), acetol ($Y_{500,acetol}$ = 3%) and acetaldehyde ($Y_{500,acetaldehyde}$ = 5.5%) at 500 °C.

There are several studies on steam reforming of glycerol over Ni/Al_2O_3 and our results are in line with literature reports. Adhikari et al. [68]. have shown Ni/Al_2O_3 is a good catalyst for the title reaction, in terms of glycerol conversion and hydrogen yield. Cheng et al. [69] . report H_2, CO_2 and CO as the main gaseous products over Ni/Al_2O_3, at the temperature range of 450–550 °C. They observed H_2:CO_2 ratios lower and H_2/CO ratios higher than in the current study as they have used lower Steam/Carbon ratios. In general, at higher steam to glycerol molar ratios, higher conversion and selectivity to hydrogen can be achieved [14,69,70]. Also in accordance with literature, addition of lanthana hindered the production of oxygenates and olefins in favor of CO, CO_2 and H_2 [34,35,62] . In addition, as Iriondo et al. [34]. have observed, Ni dispersion is not clearly related with catalytic activity and selectivity toward hydrogen.

3.3. Characterization of used catalysts and carbonaceous deposits.

The catalysts, exposed to reaction conditions for three hours as described above, were analyzed by XRD and TEM in order to investigate possible changes in their structure and the size of nickel particles and to define the type of carbonaceous deposits on the catalyst surface. XRD analysis has shown that there were no significant alterations regarding the crystalline phases of the used catalysts and/or size of Ni^0 crystallites for all temperatures and catalysts composition (Fig. 2B). In fact, slightly smaller particles were calculated for the used catalysts than the corresponding reduced catalyst (Table 2). Although the difference is small, it is larger than the estimated experimental error and it is observed for all materials. For some of the used catalysts (randomly selected), the Ni^0 particles size was also measured from the TEM micrographs which confirm the above observation. The particle size distribution of Ni^0 in NiAl after reduction and after 3 h exposure to reaction conditions at 600 °C are shown in Fig. 8, as an example. The Ni^0 particle size distribution in the used catalyst is narrower and shifted to smaller values. A plausible explanation is the fracture of nickel particles under reaction condition probably in the process of carbon formation.

The characteristic XRD peak of graphitic carbon is observed and it is more important for NiAl (Fig. 2B). TEM micrographs confirm the presence of filamentous carbon which is formed from graphene sheets and, thus, it is of graphitic nature (Fig. S6). As it can be seen in Fig. 2B, after 3 h under reaction conditions at 400 °C graphitic carbon (2θ = 26.3°) is clearly observed for NiAl, being less for NiBAl and much less for NiLaAl. This result is quite interesting as NiLaAl is the most active for the production of H_2, CO and CO_2 at this low temperature (Fig. 7) although nickel dispersion on the surface of this catalyst is not the highest as the calculated average metal particle size is larger than that of the other catalysts. The formation of carbon is a major issue in reforming reactions and many research efforts have been devoted in order to define the parameters which affect coking. For methane reforming reactions, the nickel particle size seems to be related to the rate of carbon deposition, the smaller the nickel particles the lesser the graphitic carbon formed [43,71 and references therein]. This is not observed in the current case, probably because the LaAl support plays a significant role in hindering coke formation [72].

The quantitative analysis of carbonaceous deposits was performed by TPH followed by TPO (Fig. S7). The amount of carbon formed ($g\,C/g_{cat}$) was determined by integration of the hydrogenation and oxidation profiles. At the reaction temperature of 400 °C, NiLaAl forms the largest amount of resilient carbon (type A), removed by TPH up to 750 °C, whereas the more refractory car-

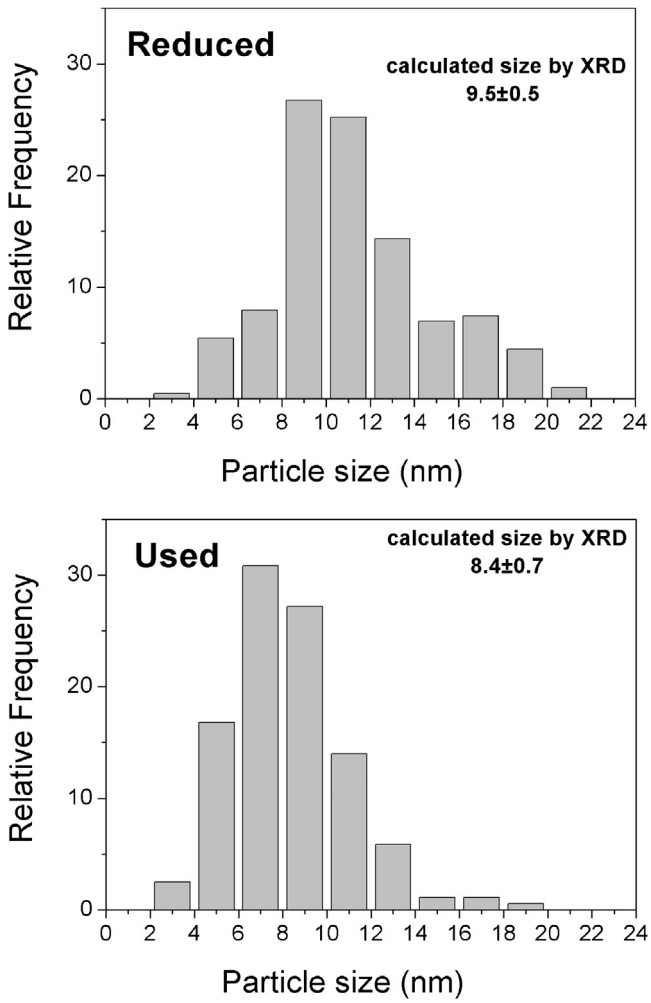

Fig. 8. Particle size distribution of Ni^0 in NiAl measured from TEM micrographs after reduction and after reaction at 600 °C for 3 h.

bon (type B), removed by TPO, is much less on this catalyst (Fig. S7). The opposite is observed for NiAl catalyst, on which a larger quantity of carbon difficult to remove is formed. NiBAl forms a similar amount of resilient carbon but much less of type B carbon. As reaction temperature increases, the amount of type A carbon decreases (Fig. S7). Type B carbon also decreases but to a smaller extent and higher temperatures are needed for its removal. At 400 °C the higher amount of coke (total carbon = typeA + type B) is formed over NiAl (Fig. 9). Even though B_2O_3 suppresses carbon formation at this temperature, it does not have the same effect at higher temperatures. On the contrary, in the presence of La_2O_3 coking is hindered at all temperatures (Fig. 9). As the catalytic tests have shown, it is possible that a different reaction path is followed in the presence of La_2O_3 and/or $LaAlO_3$ which does not involve deep dehydration reactions but fast CC breaking and CO formation followed by WGS reaction to produce more H_2 and CO_2. At 600 °C less carbon is formed for all catalysts. This is not surprising as at higher reaction temperatures and in the presence of excess water, carbon gasification (endothermic reaction) is favored and lower amounts of coke are formed [71].

3.4. Stability assessment

The stability of the NiAl and NiLaAl was investigated under more harsh conditions, i.e., lower W/F = 0.67 mg min/mL, in order to provoke and detect rapid deactivation. In fact, several W/F were explored and the one for which one of the two catalysts was deactivated after a short time on stream was selected. NiAl and NiLaAl catalysts were chosen based on the previous results, as they have been proven more effective in hydrogen production. The catalysts remained under reaction conditions at 600 °C until their initial activity (estimated from glycerol conversion) dropped to 30%. The initial activity of NiLaAl, expressed as total conversion, is similar to that of NiAl but conversion to gas products is significantly lower (Fig. 10A). A dramatic deactivation with time-on stream is observed for NiLaAl, reaching a 30% conversion in 18 h. NiAl preserves 100% total conversion for 25 h, although conversion to gas decreases slowly. Hydrogen and carbon dioxide are the main gas products and their yields follow the same trend (Fig. 10B). Carbon monoxide yield is always ca. 10%, irrespectively of glycerol con-

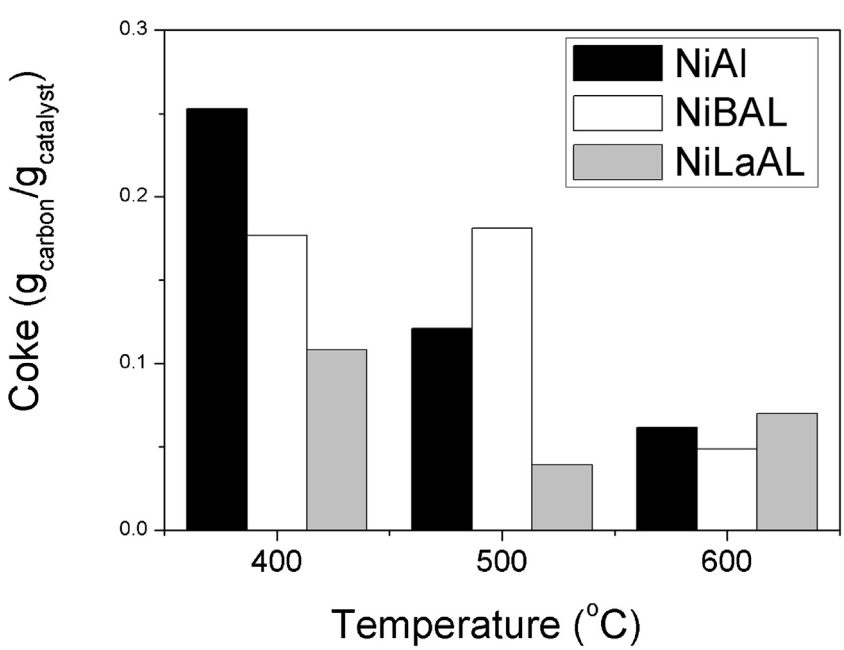

Fig. 9. Total amount of coke formed over the catalysts after 3 h under reaction conditions at 400, 500 and 600 °C (fresh catalyst was used for each temperature).

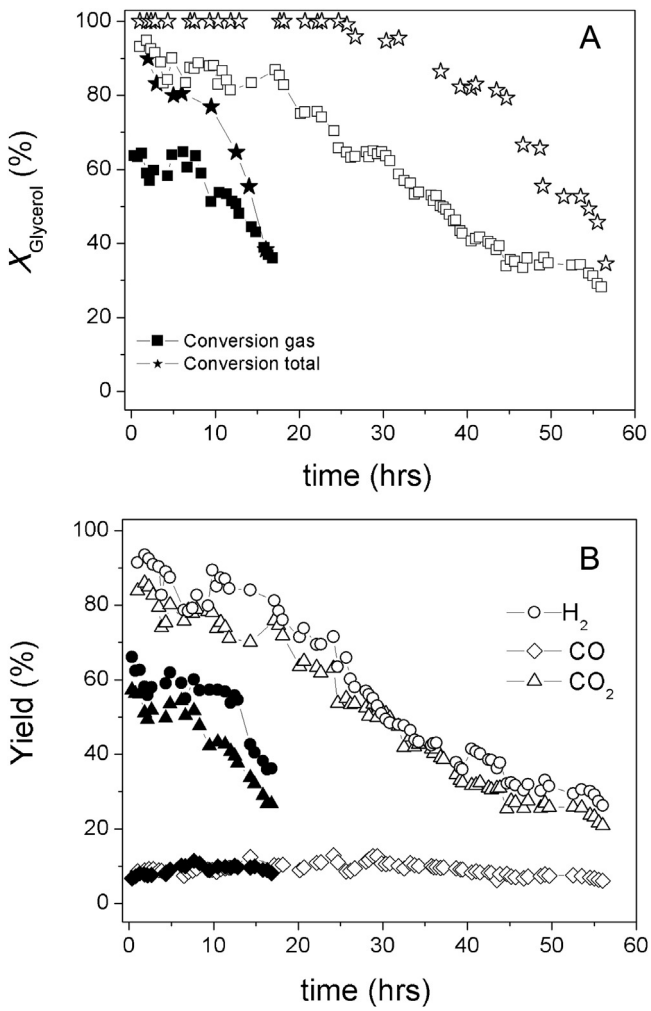

Fig. 10. Catalytic performance of NiAl (white symbols) and NiLaAl (black symbols) with time on stream at 600 °C. (A) Glycerol total conversion (⋆) and conversion to gas (■), (B) Yields (*Y*%) of main gas products H_2 (●), CO (◆) and CO_2 (◄).

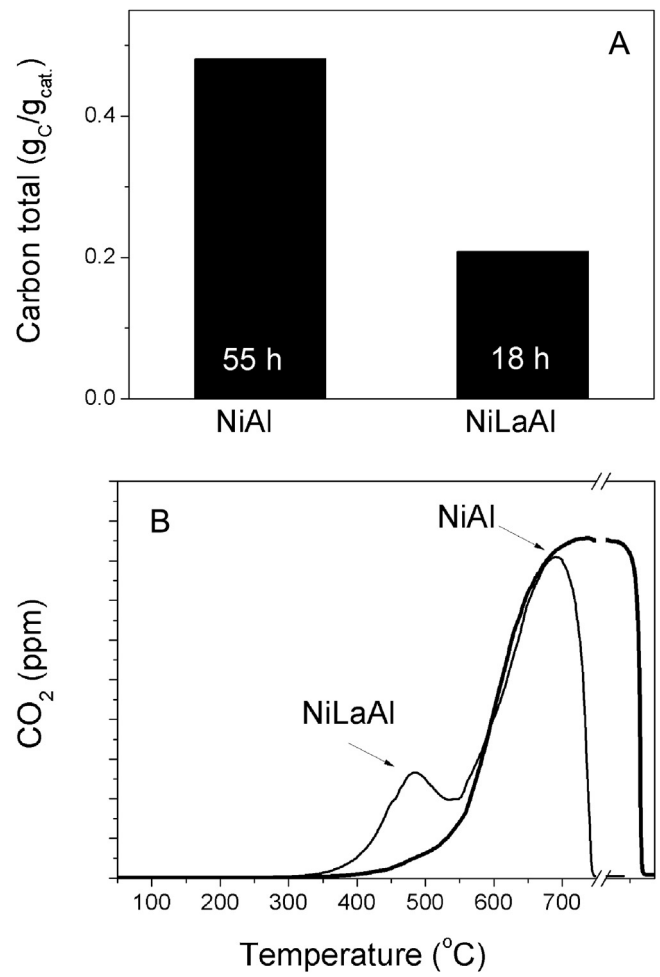

Fig. 11. Characterization of used catalysts after stability tests: (A) Total amount of coke formed, (B) TPO profiles.

version or catalyst composition, indicating that WGS reaction is at equilibrium under these reaction conditions and La_2O_3 is not important for this reaction.

The reason of NiAl deactivation is likely the formation of graphitic carbon as was detected by XRD (Fig. S8) and was measured by TPO (Fig. 11). In addition, sintering of Ni^0 particles was observed for NiAl catalyst characterized after 55 h under reaction conditions as the average Ni^0 particle size increased to 16.1 ± 0.7 nm from 9.5 ± 0.5, measured for the reduced catalyst. However, the reasons for the fast deactivation of NiLaAl are not clear. As revealed by XRD and TPO, the amount of graphitic carbon is much less and a new type of carbon, removed at lower temperatures under TPO, is formed. Nevertheless, considering the lower SSA of this catalyst, it is possible that the surface is covered by the carbonaceous deposits faster. In fact, NiLaAl catalyst having almost half the SSA of NiAl (Table 1), presents the same degree of deactivation (30% glycerol conversion) after the amount of coke formed (0.21 g C/g_{cat}) is almost half of that formed on NiAl (0.47 g C/g_{cat}). Metal phase sintering occurred at a lower degree, Ni^0 particle size increased from 11.7 ± 0.4 (reduced catalyst) to 14.2 ± 0.6 nm after 18 h under reaction conditions. Another approach was also explored in order to define whether steam could also be responsible for the quick deactivation of NiLaAl. The specific test was performed with a reaction feed containing only water and He. The SSA of NiLaAl after 3 h at 600 °C under flow of steam decreased to 68 m^2/g, which indicates that deterioration of the textural properties under reaction conditions may also contribute to catalyst deactivation. Under the same conditions the texture of NiAl also deteriorates, the specific surface area measured to be 135 m^2/g. Yet, it is still twice that of NiLaAl.

TEM migrographs show the presence of filamentous carbon on both catalysts (Fig. S9). In the case of NiAl it has a structure of carbon nanowires whereas carbon nanotubes of various diameters are formed on NiLaAl.

3.5. Coking vs acidity

The group of Adesina [69], performing a mechanistic study, concluded that a Langmuir–Hinshelwood (LH) mechanism is followed, involving the molecular adsorption of glycerol and the dissociative chemisorption of steam on two different sites (strong acid and basic sites) with surface reaction as rate determinant step. Thus, surface acidity is required to improve catalysts efficiency. On the other hand, it is generally observed that acidic supports promote dehydration, dehydrogenation, hydrogenolysis and condensation reactions which lead to coke formation and fast deactivation of the catalyst [18,73]. Cheng et al. [69]. also reported that carbon deposition was significant at 500 °C, even under excess steam condition. So, a question arises whether acidity is determining activity as well as rate of carbon formation.

Studying the impact of support's acidity for the steam reforming of glycerol over Pt-based catalysts at 350 °C, Sad et al. [18]. report that non-acidic supports favor the production of gaseous products

and consequently the production of H_2 whereas acidic supports such as Al_2O_3 decrease glycerol conversion, enhancing dehydration and dehydrogenation reactions to oxygenates such as acrolein, acetol, 1,2-propanediol, acetic acid and acetaldehyde. Nevertheless, Pt/MgO, displaying the highest basicity, is not stable with time on stream, although the reason of its deactivation is not clear as coke formed on this catalyst is low [18]. Adhikari et al. [74] . have investigated the catalytic performance of Ni/TiO_2, Ni/CeO_2 and Ni/MgO for the steam reforming of glycerol under similar reaction temperatures (550–650 °C). They report 100% glycerol conversion for Ni/CeO_2 and Ni/MgO but lower for Ni/TiO_2, whereas hydrogen yield follows the order Ni/CeO_2 > Ni/MgO > Ni/TiO_2 and carbon formation exactly the opposite order [74]. Taking into account the surface acidity of the supports (MgO < CeO_2 < TiO_2 [29]), it is clear that coke formation is not straightforwardly related with the acidity as other catalysts features are also important.

Lanthana hinders the formation of oxygenates and olefins, considered as coke precursors, as observed in the current study and reported in the literature [34,35,62]. The role of lanthana in hindering the accumulation of carbonaceous deposits may not depend only on the promotion of a different reaction pathway. According to Tsipouriari and Verykios [72] , CO_2 interacts with La_2O_3, forming $La_2O_2CO_3$ species. The latter reacts with carbon deposited onto Ni particles and at the interface between Ni and $La_2O_2CO_3$, according to the following reaction (* is an active site on the surface of Ni^0):

$$La_2O_2CO_3 + C - * \rightarrow 2CO + La_2O_3 + * \quad (11)$$

Carbon is converted to CO and is removed from the nickel surface before diffusing to graphene forming centers, whereas Ni^0 active sites and La_2O_3 are restored and available for a new catalytic cycle [72]. The rate of the above reaction is crucial defining the resistance toward coking [72]. On the other hand, at higher reaction temperatures and in the presence of water, carbon gasification (endothermic reaction) is favored and lower amounts of coke are formed over all catalysts [71].

Summarizing, catalysts exhibiting surface acidity exhibit a high rate of coke formation but basic supports do not seem to be more resistant to deactivation, although coking may not be the main reason [18,74,75]. This conclusion is in accordance with the observations of the present study which show inferior stability with time-on stream although lower amount of surface carbon is formed. It has been suggested that metal catalysts supported on neutral supports proved to be more resistant to coking [18,73].

4. Conclusions

Glycerol steam reforming was investigated over Ni dispersed on Al_2O_3, La_2O_3–Al_2O_3 and B_2O_3–Al_2O_3 catalysts as well as over bare supports. Materials were characterized using various techniques, aiming to define those properties of the catalysts which have the most significant impact on catalytic performance.

The addition of La_2O_3 onto alumina and calcination at 900 °C had a detrimental impact on the textural properties, mainly due to formation of $LaAlO_3$ phase. Acidity also decreased and this is the main factor defining its catalytic behavior, as conversion to gaseous products and acetol yield increased while acrolein yield decreased. Addition of B_2O_3 did not change significantly the texture but increased considerably acidity and selectivity to liquid products, promoting mainly the production of acrolein. Differences on catalytic behavior are more pronounced at lower temperatures.

Ni catalysts preserve the morphology and the acidity of the corresponding support, except for a small decrease in SSA for all catalysts and in acidity for NiBAl. Changes in the electronic environment of nickel were provoked by the modifiers but, besides Ni^0, no other nickel containing phases could be detected in the reduced catalysts. Ni^0 dispersion follows the order NiLaAl < NiAl < NiBAl. The addition of nickel increased significantly H_2 and CO_2 yields, even at 500 °C. However at 400 °C and 500 °C the composition of the liquid products is similar to that of the corresponding supports. Conversion to gas-phase products and hydrogen yield are enhanced by the addition of La_2O_3 to the support while the opposite is observed upon addition of B_2O_3. These differences are more pronounced at lower temperatures. Lower amount of graphitic carbon was formed on NiLaAl at all temperatures. However, this catalyst has not been proven more stable than the unmodified NiAl, mostly due to its poorer textural properties.

Acknowledgments

This study has been co-financed by the EU (European Social Fund—ESF) and Greek national funds through the Operational Program "Education and Lifelong Learning" of NSRF—Research Funding Program: Thales. Investing in knowledge society through the European Social Fund (Glycerol2Energy project, MIS 379333).

Appendix A. Supplementary data

Supplementary data associated with this article can be found, in the online version, at http://dx.doi.org/10.1016/j.apcata.2015.11.047.

References

[1] Energy, Electricity and Nuclear Power estimates for the period up to 2050, Reference data series no. 1, 2013 Edition, International Atomic Energy Agency, Vienna, 2013 http://www.iaea.org/OurWork/ST/NE/Pess/assets/rds1-33_web.pdf, accessed (15.06.15).
[2] International Energy Outlook 2013 U.S. Energy Information Administration, July 2013, http://www.eia.gov/forecasts/ieo/pdf/0484(2013).pdf accessed (15.06.15).
[3] European Biodiesel Board, http://www.ebb-eu.org/stats.php.
[4] Commission Staff Working Document, accompanying the document Report from the Commission to the European Parliament and the Council: Renewable energy progress report Brussels, accessed (27.03.13).
[5] M. Pagliaro, R. Ciriminna, H. Kimura, M. Rossi, C.D. Pina, Eur. J. Lipid Sci. Technol. 111 (2009) 788–799.
[6] P.D. Vaidya, A.E. Rodrigues, Chem. Eng. Technol. 32 (2009) 1463–1469.
[7] M. Ayoub, A.Z. Abdullah, Renew. Sust. Energy Rev. 16 (2012) 2671–2686.
[8] K. Pathak, K.M. Reddy, N.N. Bakhshi, A.K. Dalai, Appl. Catal. A 372 (2010) 224–238.
[9] P. Panagiotopoulou, C. Papadopoulou, H. Matralis, X. Verykios, WIREs Energy Environ. 3 (2014) 231–253.
[10] D. Stosic, S. Bennici, S. Sirotin, C. Calais, J.L. Couturier, J.L. Dubois, A. Travert, A. Auroux, Appl. Catal. A: Gen. 447–448 (2012) 124–134.
[11] D. Hernandez, M. Velasquez, P. Ayrault, D. Lopez, J.J. Fernandez, A. Santamaria, C. Batiot-Dupeyrat, Appl. Catal. A: Gen. 467 (2013) 315–324.
[12] M. Pagliaro, R. Ciriminna, H. Kimura, M. Rossi, C. Della Pina, Angew. Chem. Int. Ed. 46 (2007) 4434–4440.
[13] K.S. Avasthi, R.N. Reddy, S. Patel, Procedia Eng. 51 (2013) 423–429.
[14] E.A. Sanchez, M.A. D'Angelo, R.A. Comelli, Int. J. Hydrogen Energy 35 (2010) 5902–5907.
[15] F. Pompeo, G.F. Santori, N.N. Nichio, Catal. Today 172 (2011) 183–188.
[16] A. Iriondo, V.L. Barrio, M. El Doukkali, J.F. Cambra, M.B. Guemez, J. Requies, P.L. Arias, M.C. Sanchez-Sanchez, R. Navarro, J.L.G. Fierro, Int. J. Hydrogen Energy 37 (2012) 2028–2036.
[17] B.C. Miranda, R.J. Chimentao, J.B.O. Santos, F. Gispert-Guirado, J. Llorca, F. Medina, F. López Bonillo, J.E. Sueiras, Appl. Catal. B: Environ. 147 (2014) 464–480.
[18] M.E. Sad, H.A. Duarte, Ch. Vignatti, C.L. Padro, C.R. Apesteguıa, Int. J. Hydrogen Energy 40 (2015) 6097–6105.
[19] E.A. Sanchez, R.A. Comelli, Int. J. Hydrogen Energy 39 (2014) 8650–8655.
[20] L.F. Bobadilla, A. Penkova, A. Álvarez, M.I. Domínguez, F. Rome ro-Sarria, M.A. Centeno, J.A. Odriozola, Appl. Catal. A: Gen. 492 (2015) 38–47.
[21] J.M. Silva, M.A. Soria, L.M. Madeira, Renew. Sust. Energy Rev. 42 (2015) 1187–1213.
[22] S. Adhikari, S.D. Fernando, A. Haryanto, Energy Convers. Manag. 50 (2009) 2600–2604.
[23] L.F. Bobadilla, A. Alvarez, M.I. Dominguez, F. Romero-Sarri, M.A. Centeno, M. Montes, J.A. Odriozola, Appl. Catal. B: Environ. 123–124 (2012) 379–390.
[24] A. Iriondo, V.L. Barrio, J.F. Cambra, P.L. Arias, M.B. Guemez, M.C. Sanchez-Sanchez, R.M. Navarro, J.L.G. Fierro, Int. J. Hydrogen Energy 35 (2010) 11622–11633.

[25] M.L. Dieuzeide, M. Jobbagy, N. Amadeo, Catal. Today 213 (2013) 50–57.
[26] L.P.R. Profeti, E.A. Ticianelli, E.M. Assaf, Int. J. Hydrogen Energy 34 (2009) 5049–5060.
[27] S.H. Kim, J.S. Jung, E.H. Yang, K.Y. Lee, D.J. Moon, Catal. Today 228 (2014) 145–151.
[28] F.S. Subramanian, M.S. Chattha, C.R. Peters, J. Mol. Catal. 69 (1991) 235–245.
[29] F. Pinna, Catal. Today 41 (1998) 129–137.
[30] D. Stosic, S. Bennici, S. Sirotin, P. Stelmachowski, J.L. Couturier, J.L. Dubois, A. Travert, A. Auroux, Catal. Today 226 (2014) 167–175.
[31] T. Horiuchi, H. Hidaka, T. Fukui, Y. Kubo, M. Horio, K. Suzuki, T. Mori, Appl. Catal. A: Gen. 167 (1998) 195–202.
[32] R. Martınez, E. Romero, C. Guimon, R. Bilbao, Appl. Catal. A: Gen. 274 (2004) 139–149.
[33] C. Melchor-Hernandez, A. Gomez-Cortes, G. Diaz, Fuel 107 (2013) 828–835.
[34] A. Iriondo, V.L. Barrio, J.F. Cambra, P.L. Arias, M.B. Goemez, R.M. Navarro, M.C. Sanchez-Sanchez, J.L.G. Fierro, Catal. Commun. 10 (2009) 1275–1278.
[35] G. Garbarino, C. Wang, I. Valsamakis, S. Chitsazan, P. Riani, E. Finocchio, M. Flytzani-Stephanopoulos, G. Busca, Appl. Catal. B: Environ. 174–175 (2015) 21–34.
[36] M. Houala, B. Delmon, Appl. Catal. 1 (1981) 285–289.
[37] G. Garbarino, E. Finocchio, A. Lagazzo, I. Valsamakis, P. Riani, V. Sanchez Escribano, G. Busca, Appl. Catal. B: Environ. 147 (2014) 813–826.
[38] S.A. Giraldo, A. Centeno, Catal. Today 133–135 (2008) 255–260.
[39] G. Colorio, J.C. Vedrine, A. Auroux, B. Bonnetot, Appl. Catal. A: Gen. 137 (1996) 55–68.
[40] Y. Guo, X. Liu, M.U. Azmat, W. Xu, J. Ren, Y. Wang, G. Lu, Int. J. Hydrogen Energy 37 (2012) 227–234.
[41] A.N. Fatsikostas, X.E. Verykios, J. Catal. 225 (2004) 439–452.
[42] V.A. Tsipouriari, A.M. Efstathiou, X.E. Verykios, J. Catal. 158 (1996) 51–63.
[43] A. Fouskas, M. Kollia, A. Kambolis, Ch. Papadopoulou, H. Matralis, Appl. Catal. A: Gen. 474 (2014) 125–134.
[44] I. Carazeanu Popovicia, V. Ciupina, G. Prodan, M.A. Girţu, J. Optoelectron. Adv. Mater. 10 (2008) 2942–2946.
[45] A. Barrera, S. Fuentes, M. Viniegra, M. Avalos-Borja, N. Bogdanchikova, J. Campa-Molina, Mater. Res. Bull. 42 (2007) 640–648.
[46] S. Palma, L.F. Bobadilla, A. Corrales, S. Ivanova, F. Romero-Sarria, M.A. Centeno, J.A. Odriozola, Appl. Catal. B: Environ. 144 (2014) 846–854.
[47] J.N. Diaz de Leona, V. Petranovskii, J.A. de los Reyes, G. Alonso-Nunez, T.A. Zepeda, S. Fuentes, J.L.G. Fierro, Appl. Catal. A: Gen. 472 (2014) 1–10.
[48] F. Tzompantzi, Y. Pina, A. Mantilla, O. Aguilar-Martínez, F. Galindo-Hernández, X. Bokhimi, A. Barrera, Catal. Today 220–222 (2014) 49–55.
[49] B. Scheffer, J.J. Heijeing, J.A. Moulijn, J. Phys. Chem. 91 (1987) 4752–4759.
[50] E. Heracleous, A.F. Lee, K. Wilson, A.A. Lemonidou, J. Catal. 231 (2005) 159–171.
[51] G. Garbarino, S. Campodonico, A.R. Perez, M.M. Carnasciali, P. Riani, E. Finocchio, G. Busca, Appl. Catal. A: Gen. 452 (2013) 163–173.
[52] G. Garbarino, I. Valsamakis, P. Riani, G. Busca, Catal. Commun. 51 (2014) 37–41.
[53] G. Garbarino, S. Chitsazan, T.K. Phung, P. Riani, G. Busca, Appl. Catal. A: Gen. 505 (2015) 86–97.
[54] J. Escobar, J.A. De Los Reyes, T. Viveros, Appl. Catal. A: Gen. 253 (2003) 151–163.
[55] J. Abart, E. Delgado, G. Ertl, H. Jeziorowski, H. Knozinger, N. Thiele, X. Zh Wang, E. Taglauer, Appl. Catal. 2 (1982) 155–176.
[56] R. Estevez, S. Lopez-Pedrajas, F. Blanco-Bonilla, D. Luna, F.M. Bautista, Chem. Eng. J. (2015), http://dx.doi.org/10.1016/j.cej.2015.03.018.
[57] S.S. Akarmazyan, P. Panagiotopoulou, A. Kambolis, C. Papadopoulou, D.I. Kondarides, Appl. Catal. B: Environ. 145 (2014) 136–148.
[58] A.T. Shakhtakhtinskaya, Z.M. Mamedova, F. Sh. Mutallibova, S.Z. Alieva, R.G. Mardzhanova, React. Kinet. Catal. Lett. 39 (1989) 137–140.
[59] S. Tang, L. Ji, J. Lin, H.C. Zeng, K.L. Tan, K. Li, J. Catal. 194 (2000) 424–430.
[60] K. Bizkarra, V.L. Barrio, A. Yartu, J. Requies, P.L. Arias, J.F. Cambra, Int. J. Hydrogen Energy 40 (2015) 5272–5280.
[61] R. Blom, I.M. Dahl, A. Slagtern, B. Sortland, A. Spjelkavik, E. Tangstad, Catal. Today 21 (1994) 535–543.
[62] A. Iriondo, J.F. Cambra, V.L. Barrio, M.B. Guemez, P.L. Arias, M.C. Sanchez-Sanchez, R.M. Navarro, J.L.G. Fierro, Appl. Catal. B: Environ. 106 (2011) 83–93.
[63] A. Iriondo, V.L. Barrio, J.F. Cambra, P.L. Arias, M.B. Guemez, R.M. Navarro, M.C. Sanchez-Sanchez, J.L.G. Fierro, Top Catal. 49 (2008) 46–58.
[64] J.T. Richardson, M.V. Twigg, Appl. Catal. A: Environ. 167 (1998) 57–64.
[65] V.A. Tsipouriari, Z. Zhang, X.E. Verykios, J. Catal. 179 (1998) 283–291.
[66] E. Tsukuda, S. Sato, R. Takahashi, T. Sodesawa, Catal. Commun. 8 (2007) 1349–1353.
[67] F.M. Bautista, J.M. Campelo, A. Garcia, D. Luna, J.M. Marinas, M.C. Moreno, A.A. Romero, Appl. Catal. A: Gen. 170 (1998) 159–168.
[68] S. Adhikari, S.D. Fernando, A. Haryanto, Catal. Today 129 (2007) 355–364.
[69] C.K. Cheng, S.Y. Foo, A.A. Adesina, Catal. Today 278 (2011) 25–33.
[70] S. Adhikari, S. Fernando, S.R. Gwaltney, S.D.F. To, R.M. Bricka, P.H. Steele, A. Haryanto, Int. J. Hydrogen Energy 32 (2007) 2875–2880.
[71] C. Papadopoulou, H. Matralis, X. Verykios, in: L. Guczi, A. Erdohelyi (Eds.), Catalysis: Alternative Energy Generation, Springer Science + Business Media, New York, 2012, pp. 57–129.
[72] V.A. Tsipouriari, X.E. Verykios, Catal. Today 64 (2001) 83–90.
[73] F. Pompeo, G.F. Santori, N.N. Nichio, Int. J. Hydrogen Energy 35 (2010) 8912–8920.
[74] S. Adhikari, S.D. Fernando, S.D.F. To, R.M. Bricka, P.H. Steele, A. Haryanto, Energy Fuels 22 (2008) 1220–1226.
[75] R.R. Soares, D.A. Simonetti, J.A. Dumesic, Angew. Chem. Int. Ed. 45 (2006) 3982–3985.